ACADEMIC PRESS

Available online at www.sciencedirect.com
SCIENCE DIRECT®

Journal of Catalysis 216 (2003) 165–177

JOURNAL OF CATALYSIS

www.elsevier.com/locate/jcat

In situ characterization of supported metal catalysts and model surfaces by time-resolved and three-dimensional XAFS techniques

Yasuhiro Iwasawa

Department of Chemistry, Graduate School of Science, The University of Tokyo Hongo, Bunkyo-ku, Tokyo, 113-0033, Japan

Received 7 August 2002; revised 30 September 2002; accepted 8 October 2002

Abstract

This paper emphasizes novel issues in in situ characterization techniques for catalysts and model surfaces, namely, energy dispersive X-ray absorption fine structure (DXAFS) for time-resolved structure analysis and polarization-dependent total-reflection fluorescence X-ray absorption fine structure (PTRF-XAFS) for 3D structure analysis, which have been developed in the past 5–10 years. DXAFS is a powerful technique for elucidating dynamic structural changes at active metal sites on catalyst surfaces that involve a sequence of formation and breaking of metal–metal, metal–adsorbate, and metal–support bonds; it opens a new area of structure kinetics, revealing kinetic parameters during catalytic reactions, catalyst preparations, and catalyst deactivation and regeneration. PTRF-XAFS is another powerful technique for elucidating 3D structures of active metal sites at single crystal model surfaces, determining structural parameters in three different directions independently with high surface sensitivity, which opens up a new area of catalytic structural chemistry, presenting information on asymmetric and anisotropic bond arrangements and transformations. The issues addressed in this paper are relevant to important key issues in understanding new catalytic structures and reaction mechanisms and to developing new concepts and strategies for novel catalytic materials, which can hardly be addressed by other techniques.

Keywords: In situ characterization; XAFS; XANES; EXAFS; Time resolved structure analysis; Three-dimensional structure analysis; Supported metal catalysts; Oxide surfaces; Zeolites; Molybdenum; Copper; Ruthenium cluster

1. Introduction

Chemical design of active structures and their arrangements on robust oxide surfaces and crystalline porous supports is crucial to create efficient catalysis with high performances [1–4]. Although the design of excellent catalysts has been a difficult challenge, molecular-level catalyst preparation has become realistic partly with the aid of in situ surface analysis by modern physical techniques as well as chemistry of definite precursors. Another important issue in achieving efficient catalysis is selectivity in catalytic oxidation/reduction and acid–base reactions, which has been a long-term challenge in fundamental research. While it has been recognized that regulation of reaction intermediates is critical in achieving selectivity, this issue has not been adequately addressed and is a serious subject to the field. It may be prerequisite for fulfillment of the design and high selectivity to understand the dynamic change of active structures in situ during preparation and reaction processes of catalytic materials.

Local structures of noncrystalline dispersed metal species have been extensively studied by X-ray absorption fine structure (XAFS) because it does not require long-range order of the metal species [1,5–9]. XAFS can directly provide the interatomic distances and coordination numbers between the particular metal and the surrounding atoms. Perhaps the most important requirement for applying XAFS to characterization of supported catalysts is in situ investigation of the working catalyst. Relevant structural information about the working catalyst is not always easy to obtain, since most techniques have difficulties in coping with structural complexity and the necessity to perform in situ measurements. XAFS can be a suitable technique for the structural analysis of active sites under reaction conditions because the reaction gases present in the catalytic systems do not interference with X-rays.

However, it takes several tens of minutes to measure an extended X-ray absorption fine structure (EXAFS) spectrum for dispersed species by conventional XAFS technique. So

E-mail address: iwasawa@chem.s.u-tokyo.ac.jp.

0021-9517/03/$ – see front matter
doi:10.1016/S0021-9517(02)00138-0

the conventional technique cannot monitor time-dependent structures during dynamic chemical processes. While XAFS provides structural information on metal sites dispersed on oxide supports, the information is averaged in every direction and hence it is a kind of one-dimensional structure information. Moreover, the contribution from the interface structure is often weaker than that from metal–metal bonding in the metal particles. Lack of accurate knowledge about the interface structure and the bonding between the metal sites and the support surfaces prevents deep understanding of the role of supports and the essence of support effects.

In the past 10 years two different new XAFS techniques have been developed; time-resolved energy-dispersive XAFS (DXAFS) [10–24] and polarization-dependent total-reflection fluorescence XAFS (PTRF-XAFS) [25–33], which are applied to studies of dynamic structural changes at metal sites during chemical processes and of three-dimensional asymmetric/anisotropic structures of metal sites on flat oxide surfaces, respectively.

The aim of this paper is to illustrate how these two XAFS techniques document time-resolved changes in active structures and three-dimensional bonding features in asymmetric and anisotropic structures for dispersed metal species.

2. Two advanced in situ XAFS techniques

XAFS has made progress theoretically and experimentally in the past 10 years, in addition to steady progress in the past 30 years, which can document how catalysts are assembled, how they work, and how they change during reaction.

2.1. Time-resolved energy-dispersive XAFS (DXAFS)

DXAFS is a technique for measuring the whole range of X-ray absorption spectra using a bent crystal and a position sensitive detector (1024 ch. photodiode arrays) as shown in Fig. 1. As no mechanical motion for monochromatizing X-rays is required in this technique, EXAFS spectra for catalysts can be measured every 1 s and even less than 1 s. The DXAFS technique has been applied to the elucidation of structural changes during catalyst preparation, chemical treatment, catalytic reaction [10–24], which cannot be elucidated by other time-resolved methods such as time-resolved IR, Raman, XRD, and luminescence techniques. There is another technique for time-resolved XAFS, called quick-scanning XAFS, which is achieved by using an electrical gear, resulting in very smooth quasi-continuous operation of the monochromator stepping motors [34–39]. DXAFS measurement set-up and detection may be difficult relative to quick-scanning XAFS, but DXAFS has better time-resolution capability. Since a DXAFS spectrum is measured at once without scanning the X-ray energies, it may suitable for the study of transient and short-lived catalytic species.

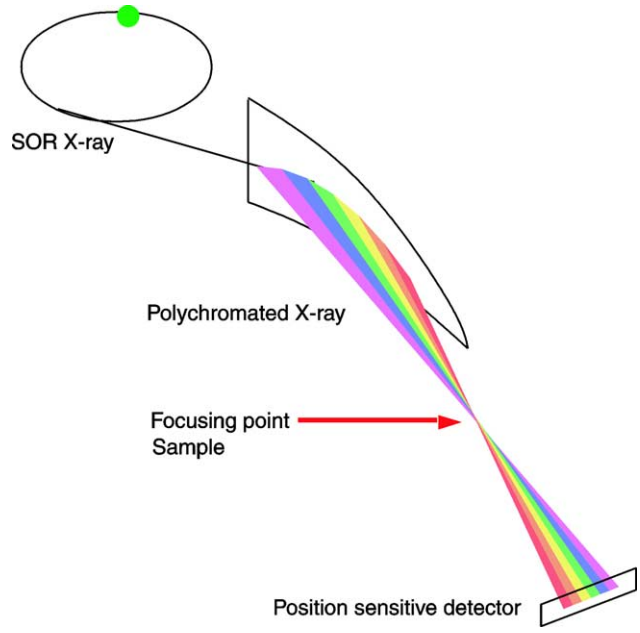

Fig. 1. Energy dispersive XAFS (DXAFS) set-up.

We have succeeded in observing and analyzing the structural changes in the temperature-programmed reduction of Cu/ZSM-5 and the temperature programmed decarbonylation of $Mo(CO)_6$/YZ by DXAFS [17,19–21].

DXAFS measurements were carried out on BL-9C at KEK-PF with a Si(311) polychromator [17]. The relationship for the curved polychromator in Fig. 1 is given by the equation [10,12,13,40–46]

$$\frac{1}{p}+\frac{1}{q}=\frac{2}{R\sin\theta_{\mathrm{B}}}, \tag{1}$$

where p, q, R, and θ_{B} are the source-to-crystal distance, the crystal-to-focus distance, the radius of curvature of the Si crystal, and the Bragg angle at the center of the crystal, respectively. The energy range (ΔE) is given by a function of $E, L, \theta_{\mathrm{B}}, R$, and p, where E and L are the energy at the center of the crystal and the length of the irradiated crystal, respectively. The X-ray absorption spectra are calculated by $\ln(I_0/I)$, where I and I_0 are X-ray intensities with and without a sample, respectively.

EXAFS data were analyzed by the UWXAFS package [47]. After background subtraction using AUTOBK [48], k^3-weighted EXAFS functions were Fourier transformed into R-space and fitted in the R-space. The backscattering amplitudes and phase shifts were calculated by the FEFF8 code [49]. The energy resolution of the spectrometer (5 eV) was taken into account to calculate the parameters by using the "EXCHANGE" flag of an input file in the FEFF8.0 code. To analyze DXAFS data, Debye–Waller factors calculated from conventional EXAFS data measured at several temperatures were used.

2.2. Polarization-dependent total-reflection fluorescence XAFS (PTRF-XAFS)

PTRF-XAFS is a technique for measuring asymmetric and anisotropic structures of metal species supported on flat oxide surfaces like single crystals in three-dimensional directions. XAFS involves polarization-dependent information from

$$\chi(k) = 3\sum \chi_i(k)\cos^2\theta_i \quad (2)$$

where $\chi(k)$, θ_i, and $\chi_i(k)$ are XAFS oscillation, angle between the ith bond and the polarization vector of the incident X-ray, and XAFS oscillation accompanying the ith bond, respectively [9,26,31,32]. Thus when one uses polarized X-rays with the electric vector perpendicular to the surface on which metal species are supported, one can get information on bonding in a direction perpendicular to the surface, while when polarized X-rays with electric vector parallel to the surface (two azimuthal directions) are used, structural information in the two in-plane directions parallel to the surface can be obtained, as shown in Fig. 2. However, it is difficult to measure the surface XAFS of a single crystal because hard X-rays penetrate deeply into the bulk substrate and the amount of surface metal species is low. The PTRF-XAFS technique can overcome this difficulty. The penetration depth of X-rays is limited to a few nm under total reflection conditions. Further, the fluorescence detection mode can obtain XAFS spectra with high sensitivity for the dilute systems.

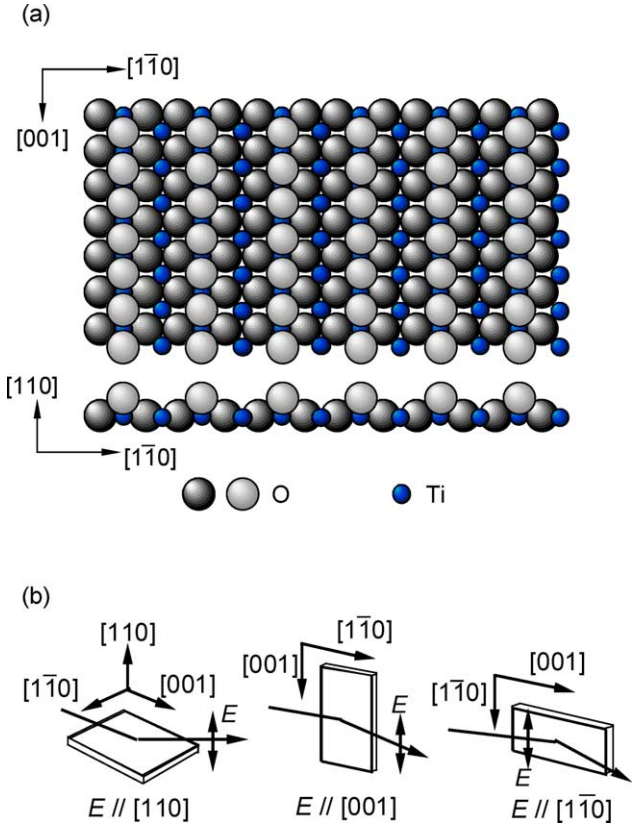

Fig. 2. Three directions for PTRF-XAFS of $Mo/TiO_2(110)$ and $Cu/TiO_2(110)$. (a) Top view and side view of $TiO_2(110)$ surface; (b) three different directions of electric vectors of X-rays to the $TiO_2(110)$ surface.

PTRF-XAFS spectra for $Mo/TiO_2(110)$ and $Cu/TiO_2(110)$ were measured in three different directions with the electric vector of the incident X-rays parallel to the [1$\bar{1}$0], [001], and [110] axes of $TiO_2(110)$ at BL14A vertical wiggler line and BL12C station of KEK-PF, respectively, as shown in Fig. 2b. The X-ray was monochromatized by a Si(111) double crystal monochromator and was focused by a bent cylindirical mirror coated with Rh metal. The X-ray beam was collimated with a 0.1-mm pinhole slit in order not to irradiate the parts, except for the sample surface. The sample was set on the rotation center of a six-axis goniometer installed in a PTRF-XAFS chamber [two different chambers for $Mo/TiO_2(110)$ and $Cu/TiO_2(110)$] [32,33,50]. By using the goniometer, one can adjust the three different orientations of the sample surface and their total reflection conditions. The fluorescent X-ray was detected by a NaI scintillation counter at the side of the chamber. EXAFS oscillations were extracted by using a AUTOBK program package [48]. The background was estimated by cubic smoothing [51] and normalized by the edge height. The Fourier transformed data were fitted with the FEFFIT program in R space [48]. Backscattering amplitude and phase shift functions were calculated using FEFF8.0 [49]. The structures of Mo and Cu species on $TiO_2(110)$ were determined to be ones which reproduce the EXAFS spectra in the three different directions at the same time. Detailed data analysis is described elsewhere [32,50].

3. Results and discussion

3.1. Time-resolved DXAFS for the dynamic structural analysis

3.1.1. Intermediates of $Mo(CO)_6/YZ$ during temperature-programmed decarbonylation

Numerous studies have been done to prepare highly dispersed metal species with uniform structures in zeolites by using metal carbonyls. Despite the past extensive study, the issues of how catalytic metal sites are produced, assembled and changed are not clear yet. This is mainly due to lack of information on the time-dependent structures during the dynamic decarbonylation processes. Fig. 3a and 3b show energy-dispersive X-ray absorption spectra at the Mo K-edge for $Mo(CO)_6/NaY$ and $Mo(CO)_6/HY$, respectively, during the temperature-programmed (TP) decarbonylation [17,19]. The DXAFS spectra were recorded every 1 s. The zeolite wafers in the XAFS cells were exposed to $Mo(CO)_6$ vapor for 24 h. The Mo loadings were 3.0 wt%, determined by ICP spectrometry (SEIKO SPS7000), and the sample thickness was regulated so that the edge jump was ca. 0.5. In $Mo(CO)_6/NaY$, the XANES shape changed at ca. 400 and 550 K, which indicates that the decarbonylation of

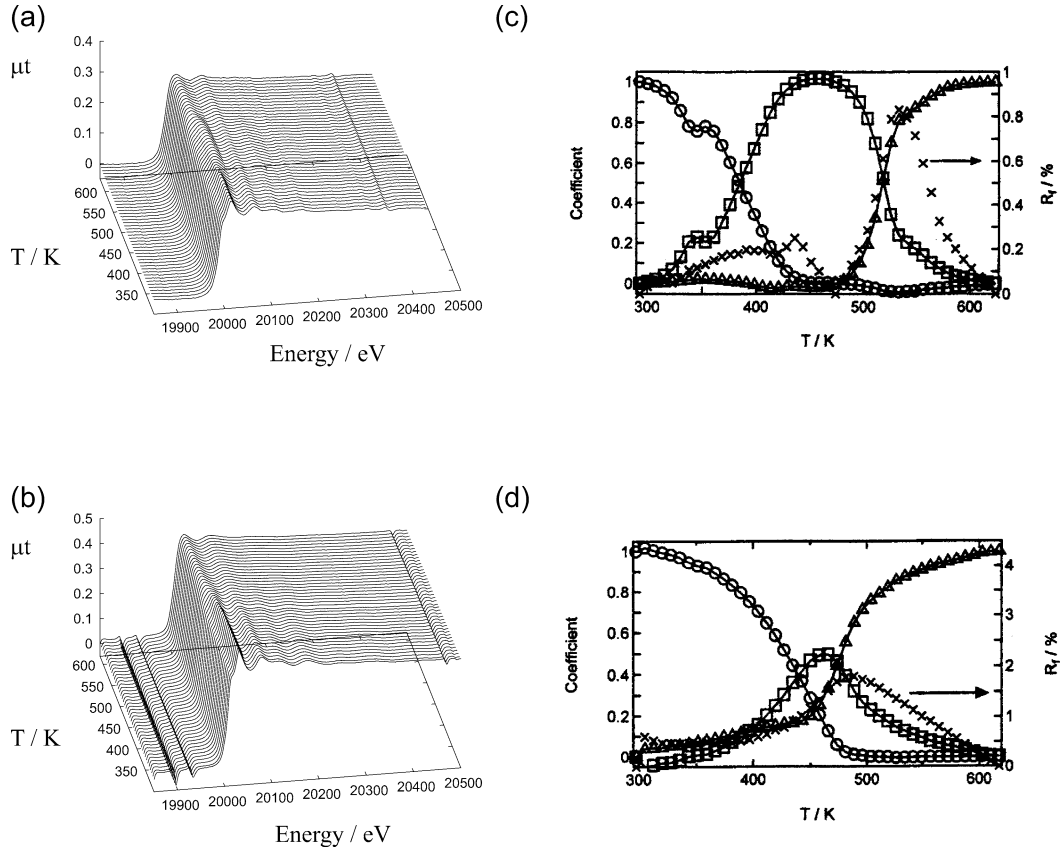

Fig. 3. (a) and (b): Time-resolved DXAFS spectra for $Mo(CO)_6$/NaY and $Mo(CO)_6$/HY, respectively, during the temperature programmed decarbonylation; (c) and (d): the coefficients in Eq. (3) for initial (circle), intermediate (square), and final (triangle) Mo species in $Mo(CO)_6$/NaY and $Mo(CO)_6$/HY, respectively, and residual factors (cross) as a function of the decarbonylation temperature. The XANES spectra at 293, 473, and 623 K were used as the spectra for the initial, intermediate, and final Mo species.

$Mo(CO)_6$/NaY proceeds through a stable intermediate existing at 400–550 K. On the other hand, in $Mo(CO)_6$/HY the XANES shape changed once around 450 K, indicating that there is no stable intermediate species during the TP decarbonylation.

To analyze the change in more detail, we have reproduced the XANES spectra during the TP decarbonylation by linear combination of reference spectra for initial (before decarbonylation at 293 K), intermediate, and final (after decarbonylation at 623 K) species,

$$X_{\text{obs}} = \sum_i C_i X_i, \tag{3}$$

where X_{obs}, C_i, and X_i are an observed spectrum, the coefficient of the ith reference spectrum, and ith reference spectrum, respectively. The XANES spectrum of $Mo(CO)_6$/NaY at 473 K was used as the reference spectrum for an intermediate species during the decarbonylation of both $Mo(CO)_6$/NaY and $Mo(CO)_6$/HY. The coefficients C_i were obtained by a linear least-squares fitting. Fig. 3c and 3d show the coefficients for Mo reference species (initial, intermediate, and final species) derived from the XANES analysis as presented in Eq. (3) [17]. As shown in Fig. 3c, all the XANES spectra for $Mo(CO)_6$/NaY during the TP decarbonylation were basically reproduced by a linear combination of the reference spectra as indicated by small residual factors (R_f) below 1%. The R_f's at 500–580 K were relatively large. In this temperature range a fractional amount of unstable intermediate species might exist but the XANES analysis cannot say anything about such fractional species. The XANES spectra for $Mo(CO)_6$/NaY were also reproduced by a linear combination of the reference spectra, as shown in Fig. 3d. However, the fraction of the intermediate species is small compared to the case of $Mo(CO)_6$/NaY and the intermediate species always coexist with the initial and final species, indicating that the intermediate is on unstable and short-lived species.

Fig. 4 shows a series of Fourier-transformed k^3-weighted EXAFS functions during the TP decarbonylation processes of $Mo(CO)_6$/NaY (a) and $Mo(CO)_6$/HY (b) [17]. The details of analysis of structural parameters for the Mo species were described in our previous paper [17]. In $Mo(CO)_6$/NaY, two peaks were observed at 0.14 and 0.26 nm (phase shift uncorrected) due to Mo–C and Mo–(C)–O bonds of Mo carbonyl species. These two peaks decreased in intensity with temperature and at ca. 400 K shifted to shorter distances and got broader. New peaks were observed up to ca. 500 K and disappeared above ca. 500 K to give

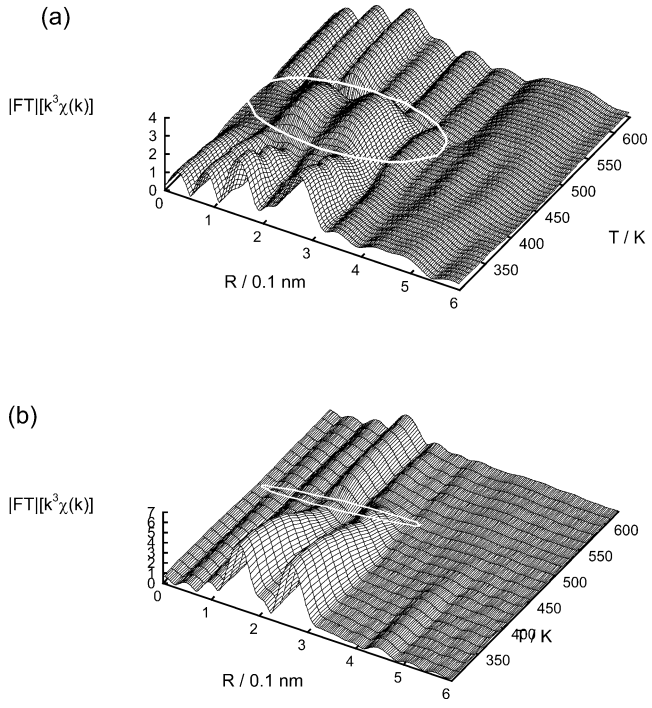

Fig. 4. A series of Fourier transformed k^3-weighted DXAFS functions during the TP decarbonylation of $Mo(CO)_6/NaY$ (a) and $Mo(CO)_6/HY$ (b). Circles show the intermediate regions.

the peaks at 0.16 and 0.26 nm (phase shift uncorrected) for the final species. The change in the DXAFS indicates that the decarbonylation process occurred via two steps and that a stable intermediate species exists in the temperature range 400–500 K as enclosed by a circle in Fig. 4a. In $Mo(CO)_6/HY$, two peaks were observed at 0.14 and 0.26 nm (phase shift uncorrected) due to Mo–C and Mo–(C)–O bonds of Mo carbonyl species. The intensity of these peaks decreased with temperature up to 420 K. At ca. 450 K, two peaks shifted to 0.12 and 0.24 nm, respectively, and disappeared above ca. 500 K. A new peak appeared at 500 K at 0.12 nm (phase shift uncorrected) and the intensity of the new peak increased with temperature. The DXAFS results indicate that a short-lived intermediate may exist around 450 K, which agrees with the results of XANES analysis in Figs. 3b and 3d.

Coordination numbers (CN) and bond distances (R) of Mo species during the decarbonylation of $Mo(CO)_6/NaY$ and $Mo(CO)_6/HY$ were determined by a curve fitting analysis of the DXAFS spectra [17]. Because there are a few species during the TP decarbonylation process and because the number of independent parameters in the DXAFS spectra is limited to 10–12, the number of fitting parameters should be reduced. To reduce the number of the fitting parameters we used Debye–Waller factors of the stable species such as $Mo(CO)_6/NaY$, $Mo(CO)_6/HY$, $Mo(CO)_3(O_L)_3/NaY$, $Mo_2(C)(O_Z)_x/NaY$, and $Mo(II)(O_Z)_2/HY$ calculated from conventional EXAFS data measured as a function of temperature [20]. The O_L and O_Z stand for lattice oxygen atoms of the zeolites. The EXAFS spectra measured at different temperature were fitted simultaneously to estimate the statistical Debye–Waller factors and the Einstein temperature of each shell. Because the bonding mode of the incipient adsorbed $Mo(CO)_6$ is of the molecule and the bonding of Mo–CO in $[Mo(CO)_3(O_L)_3]$ species can be regarded as a molecular type rather than a continuous bulk, the Einstein model was used to calculate the Debye–Waller factor of the Mo–CO contribution. Debye–Waller factors at a certain temperature were calculated by the known formula [20]. Thus, Debye–Waller factors of $Mo(CO)_6/NaY$, $Mo(CO)_6/HY$, $Mo(CO)_3(O_L)_3/NaY$, $Mo_2(C)O_x/NaY$, and $Mo(II)/HY$ can be fixed at the values calculated by the formula, and free parameters for these species are the CN and R of each shell. The CNs of Mo–C and Mo–(C)–O bonds in the Mo carbonyl species were set to an equal value. Another bond assigned to Mo–O was also observed in the TP processes, whose behavior was different from the behavior of Mo–C and Mo–(C)–O of the Mo carbonyls. Although EXAFS cannot discriminate Mo–O from Mo–C, the assignment to Mo–O was done reasonably in the present systems [20]. The determined structural parameters indicate that $Mo(CO)_3(O_L)_3$ species are formed during the TP decarbonylation of $Mo(CO)_6/NaY$ [17,19]. In the second step two $Mo(CO)_3(O_L)_3$ species merge with each other to form molybdenum oxycarbide dimer $Mo_2(C)(O_Z)_x$ [52].

The XANES analysis and the curve-fitting analysis of DXAFS spectra suggest that the decarbonylation of $Mo(CO)_6/HY$ also proceeds through subcarbonyl intermediate species. Mo–C and Mo–(C)–O bonds for the subcarbonyl intermediate species, which are significantly shorter than those of $Mo(CO)_6$ in HY, were observed in the range 400–500 K by DXAFS analysis [20]. The coordination number of the Mo–C and Mo–(C)–O in the subcarbonyl intermediate species determined by the curve-fitting analysis should be normalized by the fraction of the subcarbonyl species among total Mo species determined by the DXANES analysis in order to estimate the number of CO ligands per Mo in the subcarbonyl species. Normalized CN ((observed CN)/(fraction of the subcarbonyl species)) of the Mo–CO was about 3–4, which suggests that $Mo(CO)_{3–4}$ is formed during the decarbonylation. The intermediate species may be similar to $Mo(CO)_3(O_L)_3/NaY$ because the Mo–C and Mo–(C)–O distances for the intermediate at 0.192 and 0.309 nm are similar to those for $Mo(CO)_3(O_L)_3/NaY$. The CNs for Mo–O_L in the intermediate were about half of those for Mo–C and Mo–(C)–O of the carbonyl ligands, which indicates that the subcarbonyl species is $Mo(CO)_3(O_L)_x$ ($x = 1$–2) [17].

The intermediate species changes to the oxomolybdenum species Mo(II) $(O_Z)_2/HY$, which indicates that the $Mo(CO)_3(O_L)_x$ ($x = 1$–2) species are easily oxidized by the zeolite protons. The oxomolybdenum species in the HY supercages after the decarbonylation of $Mo(CO)_6/HY$ at 623 K can be fitted without an Mo–Mo contribution [20]. During the transformation of $Mo(CO)_3(O_L)_x/HY$ to Mo(II) $(O_Z)_2/HY$, oxidation of the molybdenum species occurs by

zeolite OH (proton). The conclusion derived from the DXAFS analysis is supported by TPD experiments [44], where desorption of H_2 is observed at 420 K [53].

Detailed study of the decarbonylation of $Mo(CO)_6$ in the Y zeolite supercages by the DXAFS technique reveals the dynamical structure change of the molybdenum species. The stability of the subcarbonyl intermediate species is different between NaY and HY. In NaY, the subcarbonyl species are stable at 400–500 K and transform to Mo oxycarbide dimeric species above 500 K; $Mo(CO)_6 \rightarrow Mo(CO)_3(O_L)_3 \rightarrow Mo_2(C)(O_Z)_x$. In the decarbonylation of $Mo(CO)_6$/HY, short-lived $Mo(CO)_3(O_L)_x$ $(x = 1–2)$ species are formed and they react readily with zeolite OH to form Mo(II) monomers and H_2: $Mo(CO)_6 \rightarrow Mo(CO)_3(O_L)_2 \rightarrow Mo(II)(O_Z)_2$. This is the first report that has elucidated the structure of short-lived intermediate species, which can be achieved by the DXAFS technique [20].

3.1.2. Structure kinetics of $[Ru_6C]/MgO$

Little is known about the dynamic properties of supported clusters, the role of a multiply bonded cluster framework, and how they work as catalysts. This may be attributed to the ambiguity of a dynamic change in the metal-framework structure at the surface under the catalytic reaction conditions. We reported the specific catalysis by $[Ru_6C]$ clusters on MgO for CO conversion to oxygenated compounds such as methanol, dimethyl ether, and formaldehyde as main products and a structural change of the cluster framework upon carbonylation and decarbonylation [54,55]. This is contrasted to catalysis by supported Ru particles, which produced methane as the main product under identical reaction conditions. The $[Ru_6C]/MgO$ catalyst was prepared by supporting a $[Ru_6C(CO)_{16}Me]^-$ cluster on MgO, followed by evacuation at 623 K as shown in Fig. 5 [54,55]. The surface area of the MgO support was 105 $m^2\ g^{-1}$ and the Ru loading on it was 4.0 wt%. When the decarbonylated $[Ru_6C]/MgO$ species with an Ru–Ru bond at 0.265 nm was exposed to CO/H_2 reaction gas at 523 K, the cluster framework expanded to a framework with the Ru–Ru bond at 0.271 nm, adsorbing 11 CO molecules per cluster. At low CO pressures the carbonylated $[Ru_6C(CO)_{11}]/MgO$ was transformed back to the original shrunken $[Ru_6C]$ framework, desorbing the CO, under which reaction conditions the reaction rate for the oxygenate synthesis was much lower than that on the expanded framework. The information on how and when the cluster structure changes upon CO adsorption/desorption will provide knowledge and understanding, at the molecular level of detail, of the origin of key factors for catalysis and the principle of design of efficient catalysts, which can hardly be obtained by other techniques. The following is the first study on the kinetics of reversible structural change in cluster framework at surface.

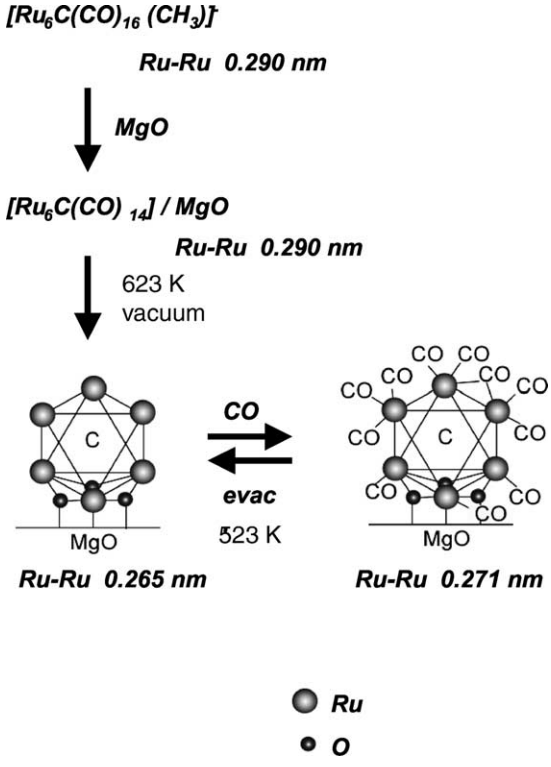

Fig. 5. Preparation steps for the supported $[Ru_6C]/MgO$ catalyst and the reversible transformations between $[Ru_6C]$ and $[Ru_6C(CO)_{11}]$ on MgO.

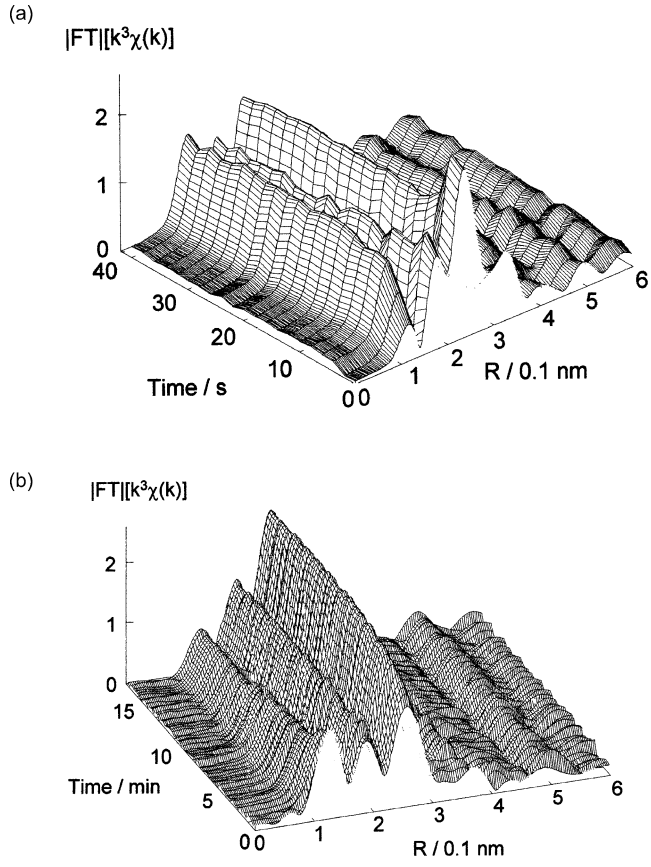

Fig. 6. (a) A series of Fourier transformed DXAFS functions at the Ru K-edge during the carbonylation of $[Ru_6C]/MgO$ under CO/H_2 at 523 K. (b) A series of Fourier transformed DXAFS functions at the Ru K-edge during the decarbonylation of $[Ru_6C(CO)_{11}]/MgO$ under vacuum at 573 K.

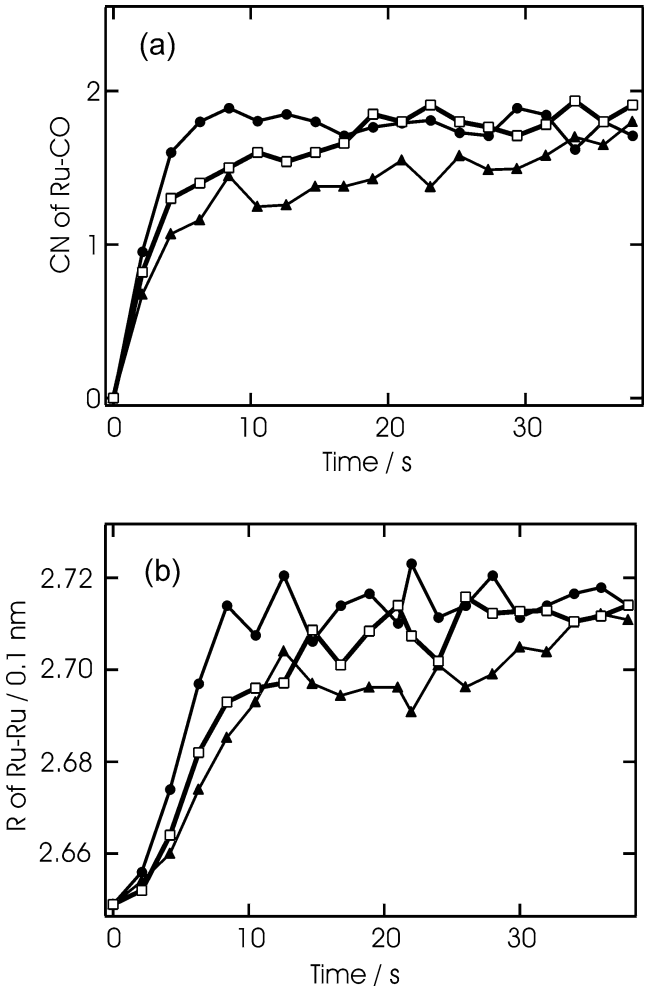

Fig. 7. The coordination numbers (CN) of Ru–CO (a) and the bond distances (R) of Ru–Ru (b) as a function of the CO exposure time in the carbonylation processes at 423 K (filled triangle), 473 K (open square), 523 K (filled circle).

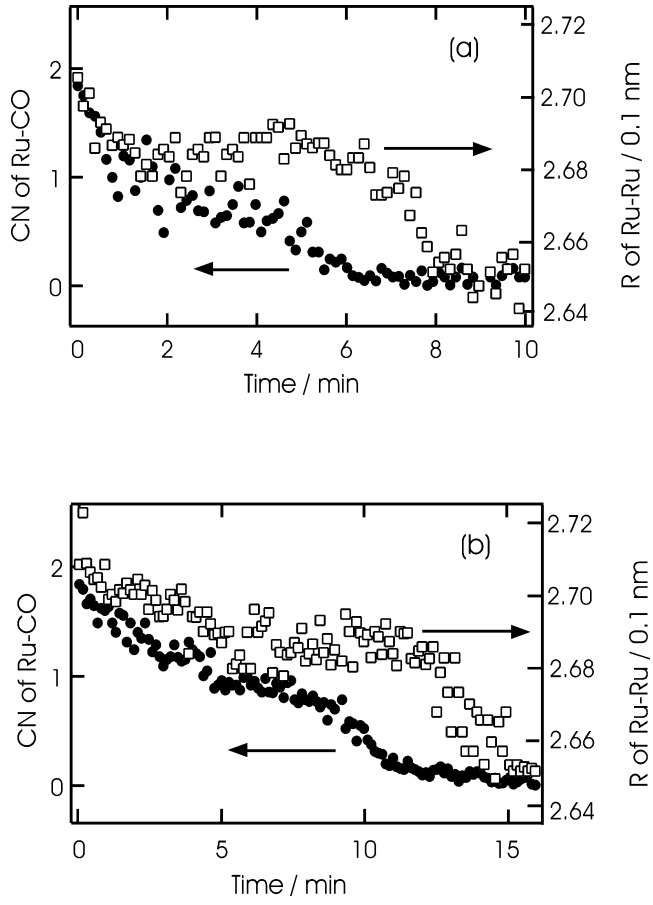

Fig. 8. The coordination numbers (CN) of Ru–CO (filled circle) and the bond distances (R) of Ru–Ru (open square) during the decarbonylation processes at 623 K (a) and 573 K(b).

Fig. 6a shows a series of Fourier-transformed DXAFS functions at the Ru K-edge during the carbonylation of $[Ru_6C]/MgO$ under CO/H_2 at 523 K. Each spectrum was measured with a time resolution of 1 s. Fig. 6b shows a series of Fourier-transformed DXAFS functions at the Ru K-edge during the decarbonylation of the carbonylated $[Ru_6C(CO)_{11}]/MgO$ under vacuum at 573 K. Each spectrum was measured with a time resolution of 2 s. The structural parameters determined by curve-fitting in R space are plotted against the carbonylation and decarbonylation time in Figs. 7 and 8. The coordination numbers (CN) of Ru–C–(O) and Ru–(C)–O for the carbonyl ligands were assumed to be the same values.

Fig. 7 shows the CN of Ru–CO (a) and the interatomic distances (R) of Ru–Ru (b) as a function of the CO-exposure period in the carbonylation processes at 423, 473, and 523 K. The CNs of Ru–C and Ru–(C)–O for the carbonyls were set to the same value in the curve fitting analysis. The error bars for R for Ru–Ru and CN for Ru–CO were ± 0.01 nm and ± 0.3–0.4, respectively. The parameters for the bonding at the cluster-support interface did not change significantly with time [56]. The CN of Ru–CO increased from 0 to 0.7 for the first 2 s at 423 K, where the R of Ru–Ru changed little. The CN of Ru–CO increased to about half of the value at saturation after 4 s, but the R of Ru–Ru almost did not yet change. After 4 s the R rapidly increased to 0.269 nm and the bond expansion was completed in 11 s at 423 K. The rates of carbonylation and bond expansion were promoted by an increase in the temperature. There were the breaks at 4–5 s in the slopes of the increase in the CN, followed by gentle slopes over 35 s. On the other hand, the slopes for the increase in the R changed at 8–11 s, followed by a gentle increase from 0.269 nm to 0.271 nm slightly over 30 s. Thus it is reasonable that we postulate the existence of two intermediate structures $[Ru_6C(CO)_6]$ with Ru–Ru distance of 0.265 and 0.269 nm during the carbonylation of $[Ru_6C]/MgO$ [47]. The number of carbonyls per cluster was also estimated by CO adsorption experiments and FTIR spectra. In the first step, six CO molecules adsorb on a $[Ru_6C]$ cluster and in the second step, following the CO adsorption, the cluster framework expands from 0.265 to 0.269 nm. After the formation of the second intermediate $[Ru_6C(CO)_6]$ with an Ru–Ru distance of 0.269 nm, CO

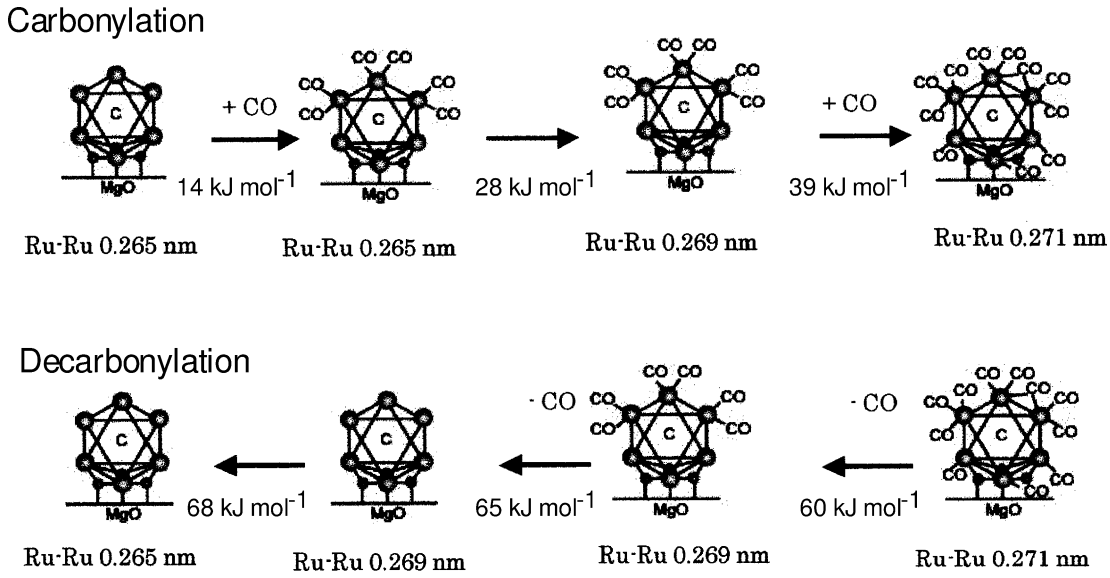

Fig. 9. The structural changes in the carbonylation and decarbonylation processes and the activation energies for the structural changes.

molecules further adsorb onto the expanded cluster, and eventually the final cluster structure $[Ru_6C(CO)_{11}]$ with 11 CO ligands and Ru–Ru distance of 0.271 nm is formed.

Fig. 8 shows the CN of Ru–CO and the *R* of Ru–Ru during the decarbonylation processes of $[Ru_6C(CO)_{11}]/MgO$ at (a) 623 K and (b) 573 K. The error bars for *R* for Ru–Ru and CN for Ru–CO were ± 0.01 nm and ± 0.2–0.3, respectively. The decarbonylation process was slower than the carbonylation process. At 623 K, the *R* of Ru–Ru changed slightly from 0.271 to 0.269 nm in 1 min, while the CN of Ru–CO decreased to about half of the original value. The *R* remained constant until 6 min, whereas the CN further decreased to zero at 6 min. After the CO desorption the *R* of Ru–Ru bond decreased from 0.269 to 0.265 nm. The cluster shrinking was completed within 3 min at 623 K, as shown in Fig. 8a. The stepwise feature of the decarbonylation was also observed at 573 K in Fig. 8b. It is reasonable that we postulate the existence of two intermediate structures $[Ru_6C(CO)_6]$ and $[Ru_6C]$ with Ru–Ru of 0.269 nm during the decarbonylation of $[Ru_6C(CO)_{11}]/MgO$ [56]. The number of carbonyls per cluster in the slow decarbonylation process was determined by FTIR. In the first step the $[Ru_6C(CO)_{11}]$ cluster is partially decarbonylated and simultaneously the framework slightly shrinks. In the second step the CO completely desorbs, whereas the *R* of the Ru–Ru bond does not change. After completion of the CO desorption, the cluster framework shrinks from 0.269 to 0.265 nm.

The structural changes in the carbonylation and decarbonylation processes are illustrated in Fig. 9, where the activation energies for each step are also shown. The activation energy for the step from $[Ru_6C]$(Ru–Ru:0.265 nm) to $[Ru_6C(CO)_6]$(0.265 nm) was determined to be 14 kJ mol^{-1} by using the rates of increase in the CN of Ru–CO, while the activation energy for the step from $[Ru_6C(CO)_6]$(0.265 nm) to $[Ru_6C(CO)_6]$(0.269 nm) was determined to be 28 kJ mol^{-1} by using the rates of the increase in the *R* of Ru–Ru bond. The activation energy for the step from $[Ru_6C(CO)_6]$ (0.269 nm) to $[Ru_6C(CO)_{11}]$(0.271 nm) was obtained by using the rates of the increases in the CN and the *R*, independently. The values determined from the CN and the *R* were 41 and 38 kJ mol^{-1}, respectively, which agreed well with each other. The activation energies for the decarbonylation processes were also determined by the DXAFS analysis. The activation energy for the step from $[Ru_6C(CO)_{11}]$(0.271 nm) to $[Ru_6C(CO)_6]$(0.269 nm) was determined to be 59 and 62 kJ mol^{-1} from the rates of the decreases in the CN of Ru–CO and R of Ru–Ru bond, respectively. Both values agreed with each other, indicating the validity of the values. The activation energy for the step from $[Ru_6C(CO)_6]$(0.269 nm) to $[Ru_6C]$(0.269 nm) was determined to be 65 kJ mol^{-1} from CN. The activation energy for the step from $[Ru_6C(CO)_6]$(0.269 nm) to $[Ru_6C]$(0.269 nm) was determined to be 65 kJ mol^{-1} from the CN. The activation energy for the step from $[Ru_6C]$(0.269 nm) to $[Ru_6C]$(0.265 nm) was determined to be 68 kJ mol^{-1} from the *R*. This sort of information on the kinetics of structural change in the cluster framework at the surface of the catalytically active site was obtained by the time-resolved DXAFS technique for the first time, which may open up a new area of kinetics of active structures at catalyst surfaces.

3.2. PTRF-XAFS for Mo dimer and Cu trimer on TiO_2(110) surfaces

3.2.1. Anisotropic Mo-dimer structure strongly interacting with TiO_2(110) surface

The PTRF-XAFS technique has been applied to Co oxides on α-Al_2O_3(0001), Cu oxide on α-quartz(0001), Pt_4 clusters on α-Al_2O_3(0001), V oxides on ZrO_2(100), and Mo oxides on TiO_2(110) [26–32,57]. The anisotropic Mo

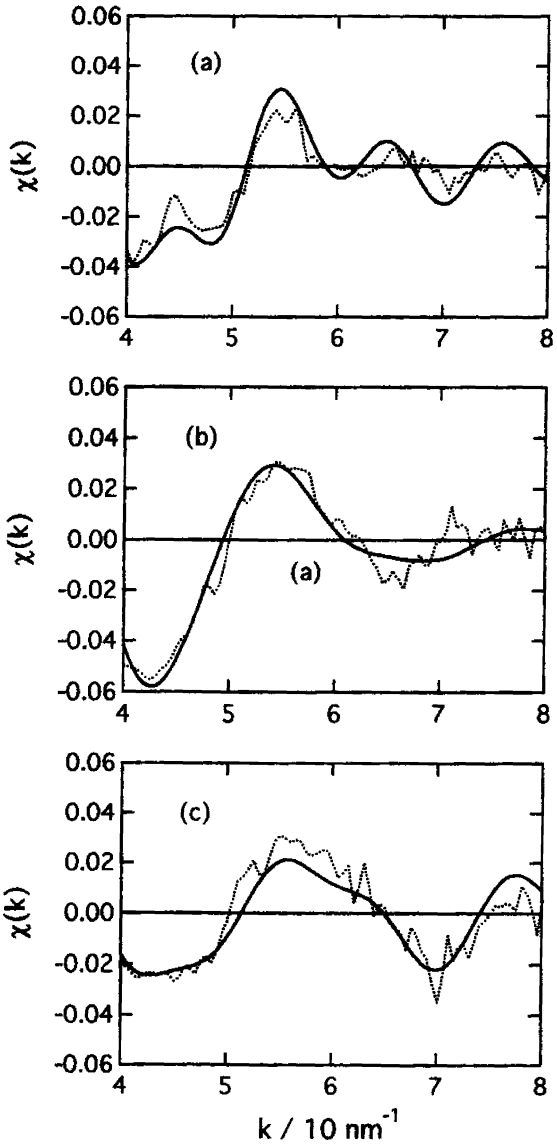

Fig. 10. PTRF-EXAFS oscillations at the Mo K-edge for Mo/TiO_2(110) and the fitting curves in the (a) [1$\bar{1}$0], (b) [001], and (c) [110] directions.

dimer structure produced on TiO_2(110) is summarized in this section.

We studied the three-dimensional structure of molybdenum oxides supported on a rutile TiO_2(110) single crystal surface as a model system for Mo/TiO_2 catalysts. Particular interest was paid to the bonding feature at the Mo–TiO_2 interface, which may decide the Mo oxide structure. A rutile TiO_2(110) surface has an anisotropic structure with alternative alignment of the protruding one-dimensional oxygen rows and the one-dimensional trough of five-fold coordinated Ti atoms along [001] axis as shown in Fig. 2a. TiO_2(110) surfaces have been well characterized by various techniques such as STM, SXRD, and ab initio calculations [58–61, Refs. in 59]. Molybdenum was supported by an impregnation method using an ultrapure aqueous solution of $(NH_4)_6Mo_7O_{24} \cdot 4H_2O$ in a quartz cell, followed by calcinations at 773 K for 3 h under O_2. The Mo loading was estimated to be 0.2 mL (1 Mo atom/nm^2) by XPS, where l mL is defined to be the same number of five-fold Ti atoms at the TiO_2(110) surface. Fig. 10 shows Mo K-edge PTRF-EXAFS spectra for Mo/TiO_2(110) with different orientations of TiO_2(110) [32]. The spectra (a)–(c) are entirely different from each other, indicating the formation of an anisotropic structure of Mo-oxide species on TiO_2(110). The short-period EXAFS oscillation in the [1$\bar{1}$0] spectrum appears in the high k-region, which suggests the presence of Mo–Mo bonding in this sample. From theoretical simulations for several hundred model structures, we succeeded in finding a structure which can reproduce the observed EXAFS oscillations in all of the three directions E//[1$\bar{1}$0], E//[001] and E//[110] as shown in Fig. 10 [32]. The model structure, which is shown in Fig. 11, has the following features. The structure is an edge-shared dimer which has an intermediate structure of the dimers in MoO_3 and $[Mo_7O_{24}]^{6-}$. The Mo–Mo distance at 0.335 nm is perpendicular to the protruding one-dimensional oxygen rows and parallel to the TiO_2(110) surface. The bond distance is a little shorter than that of the edge-shared Mo–Mo in MoO_3 and is similar to that in $[Mo_7O_{24}]^{6-}$. Two Mo atoms share the bridging oxygen atoms with the TiO_2(110) surface. The position of the bridging oxygen atoms are distorted and deviated from their original positions on TiO_2(110). The Mo dimer is located at distances of 0.218 nm up from the surface Ti plane as shown in Fig. 11. The Mo–O and Mo–Ti direct bondings at the interface were observed at distances of 0.220 and 0.296 nm, respectively. It has been demonstrated that the protruding oxygen atoms on TiO_2(110) are adsorption sites for positively charged metal atoms [62,63]. It is most likely that Mo^{6+}

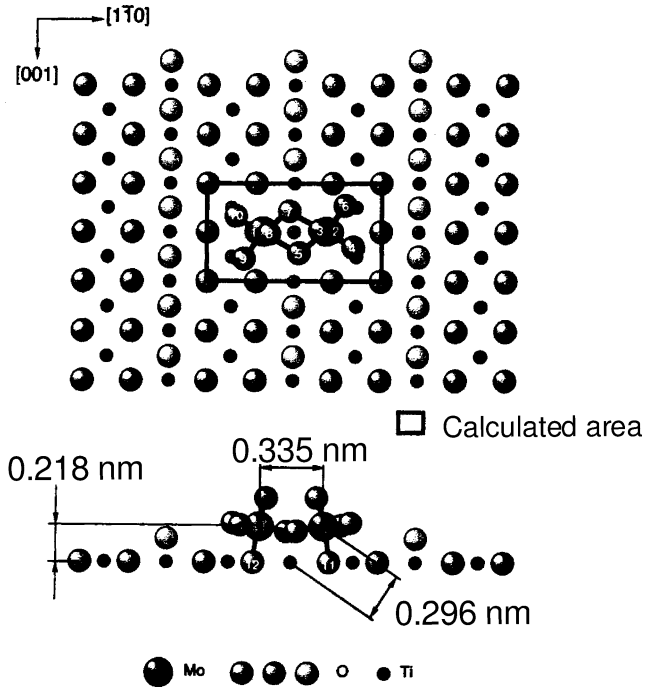

Fig. 11. A model structure of Mo–oxide dimer on TiO_2(110) (top view and side view).

Table 1
Curve-fitting results of the PTRF-EXAFS data for an as-supported $Cu/TiO_2(110)$ and of the EXAFS data for $Cu(DPM)_2$

Direction	Bond	N^*	R/nm	σ^2/nm$_2$	ΔE/eV	R_f/%
[001]	Cu–O	4.0 ± 0.4	0.194 ± 0.002	$4 \pm 2 \times 10^{-5}$	4 ± 1	2.9
$[1\bar{1}0]$	Cu–O	4.2 ± 0.4	0.193 ± 0.002	$4 \pm 2 \times 10^{-5}$	4 ± 1	3.5
[110]	Cu–O	3.8 ± 0.4	0.194 ± 0.002	$4 \pm 2 \times 10^{-5}$	4 ± 1	2.0
$Cu(DPM)_2$	Cu–O	CN = 4	$R = 0.191$ nm			

N^*: effective coordination number; R: bond distance; σ: Debye–Waller factor; ΔE: correction of edge shift; R_f: residual factor; CN: coordination number.

ions preferably interact with the protruding oxygen atoms. As shown in Fig. 11, the bridging oxygen atoms shared with Mo atoms are deviated from the original positions by strong interaction with Mo^{6+} ions [32].

The energy demerit from the distortion may be gained by chemical bonding of the bridging oxygen atoms with two Mo ions more than with a Mo ion. The distortion energy of bridging oxygen may be a key issue to form the Mo dimers attached to the oxygen ridge of $TiO_2(110)$. Further, the anisotropic topography of the $TiO_2(110)$ surface may prevent the Mo oxides from aggregating to larger clusters.

3.2.2. Inclined arrangement of Cu trimer on $TiO_2(110)$

An optically polished rutile $TiO_2(110)$ single crystal was heated at 673 K for 3 h in air, then Cu was supported on the $TiO_2(110)$ using a diethyl ether solution of $Cu(DPM)_2$, followed by H_2 reduction at 363 K, in the PTRF-XAFS chamber. The Cu loading was estimated to be 1 mL by XPS. XANES spectra for as-supported $Cu(DPM)_2/TiO_2(110)$ showed a small difference in the three directions. A shoulder was observed only in the [001] direction, though it was less clear than that for the original $Cu(DPM)_2$ complex. The shoulder at the edge has been attributed to the $1s \rightarrow 4p_\pi{}^*$ transition [64], which suggests that the edge peak is most enhanced in the direction normal to the plane of the DPM ligand. The Cu-DPM species may have a preferential alignment on $TiO_2(110)$. The XANES spectrum averaged over the three directions did not coincide with that for $Cu(DPM)_2$. These results indicate that $Cu(DPM)_2$ is supported on the $TiO_2(110)$ surface, not keeping the original structure, but probably releasing one of two DPM ligands on Cu (50). Table 1 shows the curve-fitting results of the EXAFS data in the [001], $[1\bar{1}0]$, and [110] directions for the as-supported sample. The Cu–O bond distances were estimated to be 0.194 nm for all the directions and the coordination numbers of Cu–O were about 4, indicating a tetrahedral structure, where [Cu(DPM)] species may be regarded as adsorbed on the bridge sites of the protruding oxygen atoms (Fig. 12). Adsorption of $[Rh(CO)_2]$ or $[Rh(CO)_2]Cl$ species on the protruding oxygen row of $TiO_2(110)$ has also been reported [65,66]. The detail of the structure of the as-supported $Cu(DPM)_2/TiO_2(110)$ will be reported elsewhere [50].

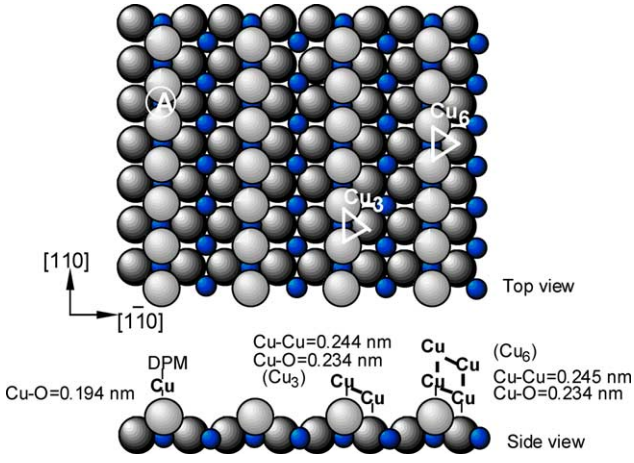

Fig. 12. Proposed location sites and structures for [Cu(DPM)] species, Cu_3 cluster, and Cu_6 cluster on $TiO_2(110)$.

Fig. 13 shows the k-weighted EXAFS oscillations in the three directions and their Fourier transforms for the sample after reduction with H_2 at 363 K. The EXAFS oscillation in

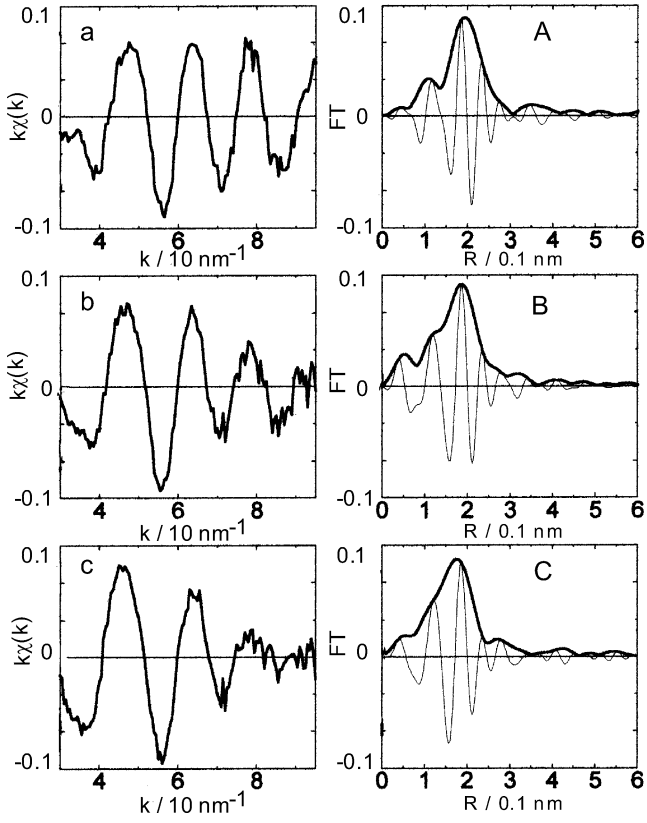

Fig. 13. PTRF-EXAFS oscillations at the Mo K-edge and their Fourier transforms in the [001] (a,A), $[1\bar{1}0]$ (b,B), and [110] (c,C) directions for $Cu/TiO_2(110)$ reduced with H_2 at 363 K.

Table 2
Curve-fitting results of the PTRF-EXAFS data for $Cu/TiO_2(110)$ reduced with H_2 at 363 K

Direction	Bond	N^*	R/nm	σ^2/nm^2	ΔE/eV	R_f/%
[001]	Cu–Cu	2.7 ± 0.3	0.244 ± 0.002	$0 \pm 2 \times 10^{-5}$	(0)	0.6
[1$\bar{1}$0]	Cu–Cu	2.0 ± 0.5	0.244 ± 0.002	(0)	(0)	5.3
[110]	Cu–Cu	0.9 ± 0.5	(0.244)	(0)	(0)	12

N^*: effective coordination number; R: bond distance; σ: Debye–Waller factor; ΔE: correction of edge shift; R_f: residual factor. Parentheses: fixed at these values.

the [110] direction damped more quickly than those in the other two directions. The peak top position of the absolute part in the Fourier transform in the [110] direction appeared at 0.174 nm (phase shift uncorrected), while the peak top positions in the [001] and [1$\bar{1}$0] directions appeared at 0.193 and 0.187 nm (phase shift uncorrected), respectively. These results suggest an anisotropic structure of the Cu sites. Table 2 shows the R-space curve-fitting results. The Cu–Cu bond distance was 0.244 nm, which is shorter by 0.015 nm than that of Cu foil. For the EXAFS in the [110] direction no good fitting results were obtained by assuming only one shell of Cu–Cu. Since the direction may involve a contribution from the substrate, Cu–O bonding may contribute to the EXAFS. To estimate the Cu–Cu contribution roughly, other parameters than the Cu–Cu coordination number were fixed in the fitting procedure (Table 2). 3D growth of Cu on $TiO_2(110)$ by reduction with H_2 at 363 K is rejected because of the small coordination number of Cu–Cu in the [110] direction. The PTRF-EXAFS demonstrates that anisotropic assembly of Cu atoms occurred on the $TiO_2(110)$ surface.

A most possible structure which reproduces the EXAFS spectra in the three directions [001], [1$\bar{1}$0], and [110] was determined by a trial and error approach by the FEFF simulation. Finally, a best simulated structure was found with an inclined Cu trimer model, as shown in Fig. 12. The Cu atoms are located atop sites of the protruding and in-plane oxygen atoms. Monomers, dimers, tetramers (2D and 3D), and other larger clusters of any structure could not reproduce the EXAFS spectra in the three directions. For trimers, linear and zigzag chain structures were also excluded. Only triangle trimers could reproduce the PTRF-EXAFS data in all of the three directions [50]. The formation of a one-atomic-layer Cu fcc(111) structure on $TiO_2(110)$ was reported in the sample prepared by metal vapor deposition, where the metal overyalers are aligned with the [001] direction [67]. The Cu trimer in Fig. 12 was not parallel to the surface and the angle between the Cu trimer plane and the [110] direction is about 30°. The inclined Cu trimer is stabilized by strong interaction between the Cu atoms and the surface oxygen atoms, as proved by the bonding of Cu–O at 0.23–0.24 nm by the FEFF simulation. The inclined arrangement of the Cu trimer reflects the anisotropic $TiO_2(110)$ surface. Atop sites of the protruding oxygen row has been theoretically predicted as the most favorable adsorption site for metal atoms [68]. The structural model is based on a nonreconstructed $TiO_2(110)$ surface. However, it has been claimed that the oxygen atoms move to the position to have stronger interaction with deposited Cu atoms [69]. In the case of the Mo dimer the protruding oxygen atoms are reconstructed by interaction with the Mo atoms [32]. The simulation revealed a best fitting of the EXAFS data in the three directions when the protruding oxygen atoms moved along the [001] direction by 0.015 nm and upward along the [110] direction by 0.01 nm [50].

The Cu trimers may be a building unit for further growth to Cu aggregates. When the inclined Cu trimer was further reduced with H_2 at 473 K, vertical growth occurred to form Cu_6 clusters with a prismatic structure, which is a double-stage structure of the Cu_3 cluster in Fig. 12 [50]. The curve-fitting results of the PTRF-EXAFS data are shown in Table 3, where the effective coordination number of Cu–Cu in the [110] direction was nearly double compared to that for the Cu_3 clusters. A self-limiting feature in the Cu_3 and Cu_6 cluster growth on $TiO_2(110)$ may be explained by lattice mismatch. The Cu–Cu distance of 0.244 nm is much shorter than the O–O distance of 0.296 nm at the $TiO_2(110)$ surface, where it is difficult for the Cu_3 and Cu_6 clusters to grow larger particles on the atop sites of the protruding oxygen atoms.

4. Future prospects

Further improvements in the synchrotron source and detection systems will make it possible to measure the changes of active structures in catalytic reaction processes over

Table 3
Curve-fitting results of the PTRF-EXAFS data for $Cu/TiO_2(110)$ reduced with H_2 at 473 K

Direction	Bond	N^*	R/nm	σ^2/nm^2	ΔE/eV	R_f/%
[001]	Cu–Cu	2.8 ± 0.5	0.245 ± 0.002	$0 \pm 2 \times 10^{-5}$	(0)	0.6
[1$\bar{1}$0]	Cu–Cu	2.5 ± 0.5	0.246 ± 0.002	$0 \pm 2 \times 10^{-5}$	(0)	1.5
[110]	Cu–Cu	1.7 ± 0.5	0.245 ± 0.002	(0)	(0)	5.3

N^*: effective coordination number; R: bond distance; σ: Debye–Waller factor; ΔE: correction of edge shift; R_f: residual factor. Parentheses: fixed at these values.

shorter times by both time-resolved DXAFS and PTRF-XAFS techniques. At the moment we can measure the DXAFS spectra for catalysts on the order of hundreds of milliseconds [70]. The change of supported metal sites in microsecond intervals will be analyzed by the DXAFS technique in the near future towards real-time in-situ characterization of catalysts. The PTRF-XAFS technique can be applied to hard-to-measure catalytic systems such as V-oxides on TiO_2 by using a 19-element solid-state detector (SSD). The accumulated knowledge of anisotropic and asymmetric structures of active metal sites at oxide surfaces, including the interfacial bondings and the time-resolved observation of their structural change under catalytic reaction conditions, may provide new concepts and strategies to develop efficient catalytic materials and systems illustrating structure kinetics and chemical design at surfaces. The trends of XAFS relevant to future progress in catalysis may be μs–ns time-resolved XAFS observation and time- and space-resolved XAFS observation for studies of dynamic aspects of the local structure at catalyst surfaces under working conditions, more precise characterization of active 3D structures on catalyst model surfaces under working conditions, characterization of each metal site with different chemical states at high resolution, more routinely reliable structural analysis of heterogeneous catalysts, more accurate theoretical analysis, etc.

Acknowledgments

The author thanks Professor K. Asakura, Professor M. Nomura, Dr. T. Shido, Dr. M. Shirai, Dr. W.-J. Chun, Dr. A. Yamaguchi, Dr. Y. Inada, and Ms. A. Suzuki (DC.2) for their helpful discussion and achievements of DXAFS and PTRF-XAFS.

References

[1] Y. Iwasawa, Adv. Catal. 35 (1987) 187.
[2] Y. Iwasawa, Stud. Surf. Sci. Catal. 101 (1996) 21. [Proceedings of the 11th International Congress on Catalsysis Baltimore.]
[3] Y. Iwasawa, Acc. Chem. Res. 30 (1997) 103.
[4] Y. Iwasawa, Catal. Today 18 (1993) 21.
[5] D.C. Koningsberger, R. Prins (Eds.), X-Ray Absorption: Principles, Applications, Techniques of EXAFS, SEXAFS and XANES, Wiley, New York, 1988.
[6] B.K. Teo, EXAFS; Basic Principles and Data Analysis, Springer, Berlin, 1986.
[7] J.C.J. Bart, G. Vlaic, Adv. Catal. 35 (1987) 1.
[8] H. Topsøe, Stud. Suf. Sci. Catal. 130 (2000) 1. [Proceedings of the 12th International Congres on Catalysis, Granada.]
[9] Y. Iwasawa (Ed.), X-Ray Absorption Fine Structure for Catalysts and Surfaces, World Scientific, Singapore, 1996.
[10] T. Matsushita, R.P. Phizackerley, Jpn. J. Appl. Phys. 20 (1981) 2223.
[11] A.M. Flank, A. Fontaine, A. Jucha, M. Lemonnier, C. Williams, J. Phys. Lett. 43 (1982) L315.
[12] A.M. Flank, A. Fontaine, A. Jucha, M. Lemonnier, D. Raoux, C. Williams, Nucl. Instrum. Meth. 208 (1983) 651.
[13] E. Dartyge, A. Fontaine, A. Jucha, D. Sayers, EXAFS and Near Edge Structure III, Springer, Berlin, 1984.
[14] J.W. Couves, J.M. Thomas, D. Waller, R.H. Jones, A.J. Dent, G.E. Derbyshire, G.N. Greaves, Nature 354 (1991) 465.
[15] G. Sanker, J.M. Thomas, D. Waller, J.W. Couves, C.R.A. Catlow, G.N. Greaves, J. Phys. Chem. 96 (1992) 7485.
[16] A. Fontaine, E. Dartyge, J.P. Itie, A. Jucha, A. Polian, H. Tolentino, G. Tourillon, Top. Curr. Chem. 151 (1989) 179.
[17] A. Yamaguchi, A. Suzuki, T. Shido, Y. Inada, K. Asakura, M. Nomura, Y. Iwasawa, J. Phys. Chem. B 106 (2002) 2415.
[18] M.A. Newton, A.J. Dent, S. Diaz-Moreno, S.G. Fiddy, J. Evans, Angew. Chem. Int. Ed. 41 (2002) 2587.
[19] A. Yamaguchi, A. Suzuki, T. Shido, Y. Inada, K. Asakura, M. Nomura, Y. Iwasawa, Catal. Lett. 71 (2001) 203.
[20] A. Yamaguchi, T. Shido, Y. Inada, T. Kogure, K. Asakura, M. Nomura, Y. Iwasawa, Bull. Chem. Soc. Jpn. 74 (2001) 801.
[21] A. Yamaguchi, T. Shido, Y. Inada, T. Kogure, K. Asakura, M. Nomura, Y. Iwasawa, Catal. Lett. 68 (2000) 139.
[22] M.A. Newton, D.G. Burnaby, A.J. Dent, S. Diaz-Moreno, J. Evans, S.G. Fiddy, T. Neisius, S. Pascarelli, S. Turin, J. Phys. Chem. A 105 (2001) 5965.
[23] S.G. Fiddy, M.A. Newton, T. Campbell, J.M. Corker, S. Turin, J. Evans, A.J. Dent, I. Harvey, G. Salvini, Chem. Commun. (2001) 445.
[24] S.G. Fiddy, M.A. Newton, A.J. Dent, G. Salvini, J.M. Corker, S. Turin, T. Campbell, J. Evans, J. Chem. Soc., Chem. Commun. (1999) 851.
[25] S.M. Heald, E. Keller, E.A. Stern, Phys. Lett. A 103 (1984) 155.
[26] M. Shirai, T. Inoue, H. Onishi, K. Asakura, Y. Iwasawa, J. Catal. 145 (1994) 159.
[27] M. Shirai, K. Asakura, Y. Iwasawa, Catal. Lett. 15 (1992) 247.
[28] M. Shirai, K. Asakura, Y. Iwasawa, Chem. Lett. (1992) 1037.
[29] K. Asakura, M. Shirai, Y. Iwasawa, Catal. Lett. 20 (1993) 117.
[30] K. Asakura, K. Tomishige, M. Shirai, W.-J. Chun, T. Yokoyama, Y. Iwasawa, Physica B 208–209 (1995) 637.
[31] K. Asakura, W.-J. Chun, M. Shirai, K. Tomishige, Y. Iwasawa, J. Phys. Chem. B 101 (1997) 5549.
[32] W.-J. Chun, K. Asakura, Y. Iwasawa, J. Phys. Chem. B 102 (1998) 9006.
[33] W.-J. Chun, Y. Tanizawa, T. Shido, Y. Iwasawa, M. Nomura, K. Asakura, J. Synchrotron Radiot. 8 (2001) 168.
[34] R. Frahm, Physica B 158 (1989) 342.
[35] R. Frahm, J. Weigelt, G. Meyer, G. Materlik, Rev. Sci. Instrum. 66 (1995) 1677.
[36] F. Cimini, R. Prins, J. Phys. Chem. B 101 (1997) 5277.
[37] J.M. Thomas, G.N. Greaves, Science 265 (1994) 1675.
[38] B.S. Clausen, Catal. Today 39 (1998) 293.
[39] J.D. Grunwaldt, A.M. Molenbroek, N.Y. Topsøe, H. Topsøe, B.S. Clausen, J. Catal. 194 (2000) 452.
[40] P.G. Allen, S.D. Conradson, J.E. Penner-Hahn, J. Appl. Crystallogr. 26 (1993) 172.
[41] P.L. Lee, M.A. Beno, G. Jennings, M. Ramanathan, G.S. Knapp, K. Huang, J. Bai, P.A. Montano, Rev. Sci. Instrum. 65 (1994) 1.
[42] J. Pellicer-Porres, A. SanMiguel, A. Fontaine, J. Synchrotron Rad. 5 (1998) 1250.
[43] M. Lemonnier, R. Fourme, F. Rousseaux, R. Kahn, Nucl. Instrum. Meth. 152 (1978) 173.
[44] E. Dartyge, A. Fontaine, G. Tourillon, R. Cortes, A. Jucha, Phys. Lett. 113 (1986) 384.
[45] R.P. Phizackerley, Z.U. Rek, G.B. Stephenson, S.D. Conradson, K.O. Hodgson, T. Matsusita, H. Oyanagi, J. Appl. Crystallogr. 16 (1983) 220.
[46] H. Tolentino, E. Dartyge, A. Fontaine, G. Tourillon, J. Appl. Crystallogr. 21 (1988) 15.
[47] E.A. Stern, M. Newville, B. Ravel, Y. Yacoby, D. Haskel, Physica B 208 (1995) 117.
[48] M. Newville, P. Livins, Y. Yacoby, E.A. Stern, J.J. Rehr, Phys. Rev. B 47 (1993) 14126.
[49] A.L. Ankudinov, B. Ravel, J.J. Rehr, S.D. Conradson, Phys. Rev. B 58 (1998) 7565.

[50] Y. Tanizawa, T. Shido, Y. Iwasawa, M. Nomura, W.-J. Chun, K. Asakura, to be published.
[51] J. Cook, D. Sayers, J. Appl. Phys. 52 (1981) 5024.
[52] K. Asakura, Y. Noguchi, Y. Iwasawa, J. Phys. Chem. B 103 (1999) 1051.
[53] Y. Okamoto, A. Maezawa, H. Kane, T. Imanaka, J. Catal. 112 (1988) 585.
[54] Y. Izumi, T. Chihara, H. Yamazaki, Y. Iwasawa, J. Phys. Chem. 98 (1994) 594.
[55] Y. Izumi, Y. Iwasawa, Chemtech 24 (1994) 20.
[56] A. Suzuki, A. Yamaguchi, T. Chihara, Y. Inada, T. Shido, K. Asakura, M. Nomura, M. Yuasa, M. Abe, Y. Iwasawa, to be published.
[57] M. Shirai, K. Asakura, Y. Iwasawa, Catal. Lett. 26 (1994) 229.
[58] G. Rohrer, V. Henrich, D. Bonnell, Surf. Sci. 278 (1992) 146.
[59] H. Onishi, K. Fukui, Y. Iwasawa, Bull. Chem. Soc. Jpn. 68 (1995) 2447.
[60] K. Fukui, H. Onishi, Y. Iwasawa, Phys. Rev. Lett. 79 (1997) 4202.
[61] H. Onishi, Y. Iwasawa, Surf. Sci. Lett. 313 (1994) L783.
[62] H. Onishi, T. Aruga, C. Egawa, Y. Iwasawa, J. Chem. Soc., Faraday Trans. 1 85 (1989) 2597.
[63] H. Onishi, Y. Iwasawa, Catal. Lett. 38 (1996) 89.
[64] N. Kosugi, in: A. Kotani (Ed.), Core Level Spectroscopy in Condensed Systems, Springer, Berlin, 1988, p. 203.
[65] J. Evans, B.E. Hayden, M.A. Newton, Surf. Sci. 462 (2000) 169.
[66] R.A. Bennett, M.A. Newton, R.D. Smith, M. Bowker, J. Evans, Surf. Sci. 487 (2001) 223.
[67] M. Wu, P. Møller, Surf. Sci. 279 (1992) 23.
[68] T. Bredow, G. Pacchioni, Surf. Sci. 426 (1999) 106.
[69] G. Charlton, P.B. Howes, C.A. Muryn, H. Raza, N. Jones, J.S.G. Taylor, C. Norris, R. McGrath, D. Norman, T.S. Turner, G. Thornton, Phys. Rev. B 61 (2000) 16117.
[70] A. Suzuki, A. Yamaguchi, M. Nomura, Y. Iwasawa, unpublished data.